JACS
JOURNAL OF THE AMERICAN CHEMICAL SOCIETY
pubs.acs.org/JACS
Article

Low-Temperature Non-Oxidative Coupling of Methane on Atomically Dispersed Titanium–Aluminum–Boron Nanopowder

Souvick Biswas, Avital Isakov, Nureshan Dias, Matthew T. Finn, Jack Cokas, Albert Epshteyn,* Anastassia N. Alexandrova,* Musahid Ahmed,* and Ralf I. Kaiser*

Cite This: J. Am. Chem. Soc. 2026, 148, 10205–10215
Read Online
ACCESS | Metrics & More | Article Recommendations | Supporting Information

ABSTRACT: Nonoxidative coupling of methane represents a long-standing challenge in heterogeneous catalysis, as it requires activation of the carbon–hydrogen (C–H) bond, controlled carbon–carbon (C–C) bond formation, and effective hydrogen management without relying on oxidants. Here, we report a low-temperature C–H activation and nonoxidative C–C coupling of methane over atomically dispersed titanium–aluminum–boron nanopowder (Ti–Al–B NP) utilizing a catalytic microreactor coupled to synchrotron single-photon photoionization reflectron time-of-flight mass spectrometry. The soft-ionization, in situ probing method detects the *nascent* reaction products and radical intermediates under operando conditions, including methyl radical, C2 hydrocarbons, and molecular hydrogen. Methane activation is initiated at 800 K, approximately 700 K below the gas-phase decomposition threshold, leading predominantly to ethylene formation with selectivity reaching up to 78% among the C–C coupled products. Electronic structure calculations on model Ti–Al–B clusters elucidate a cooperative catalytic mechanism in which titanium enables methane adsorption and C–H activation, boron acts as a reversible hydrogen reservoir, and aluminum stabilizes methylene intermediates, thereby facilitating selective C–C coupling and dehydrogenation. These findings establish a distinct catalyst architecture for nonoxidative methane coupling based on earth abundant elements alternative to expensive platinum and other noble metal-containing conventional catalysts and provide molecular-level design principles for controlling dehydrogenation and subsequent C–C bond formation in challenging light alkane conversions.

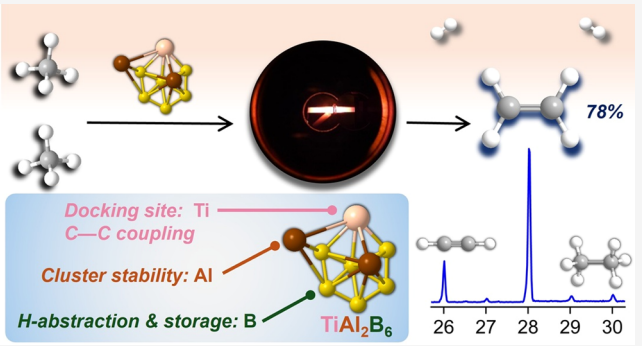

INTRODUCTION

Methane (CH_4), the dominant component of natural gas (95%) and shale gas (70%), represents both an abundant energy resource and an attractive carbon feedstock for the sustainable production of value-added chemicals.[1,2] Transforming methane into value-added chemicals via catalysis provides a compelling strategy for sustainable utilization and reducing greenhouse gas emissions; this involves, e.g., the synthesis of olefins, aromatics, and hydrogen which can essentially relieve global energy crisis.[3] However, the chemical activation of methane represents a fundamental challenge considering the high endoergicity of the sp^3 C–H bond cleavage of 439 kJ mol^{-1}, which typically requires temperatures above 1273 K.[4] The initial C–H bond cleavage constitutes the rate-determining step in the methane activation process.[5]

Traditional methane conversions rely on the oxidative coupling of methane (OCM); this strategy bears the risk of overoxidation to form carbon dioxide (CO_2), thus limiting the yield of functionalized products from methane.[6,7] Conversely, the method of nonoxidative coupling of methane (NOCM) uniquely produces hydrocarbons with two or more carbon atoms (C2+) such as ethane (C_2H_6), ethylene (C_2H_4), and acetylene (C_2H_2), alongside reported formation of propane (C_3H_8) and benzene (C_6H_6) while avoiding the concerns of oxidative couplings.[8−13] Therefore, nonoxidative couplings achieve significant economic advantages, high carbon utilization efficiency, and zero carbon dioxide emissions.[14,15] These NOCM processes require neither oxidants nor energy-expensive steps of syngas ($CO + H_2$) synthesis.[16,17] The predominant product in the NOCM is often reported to be ethane (C_2H_6), i.e., the key industrial precursor to ethylene (C_2H_4), which in turn is the most produced organic compound in the world.[18−20] Mechanistically, catalytic NOCM is proposed to involve C–H bond breaking of the adsorbed methane yielding the primary reactive methyl radical ($^{\bullet}CH_3$) intermediate, which combines and reacts further to C2+ hydrocarbons.[21]

Received: January 21, 2026
Revised: February 13, 2026
Accepted: February 18, 2026
Published: February 24, 2026

https://doi.org/10.1021/jacs.6c01503
J. Am. Chem. Soc. 2026, 148, 10205–10215

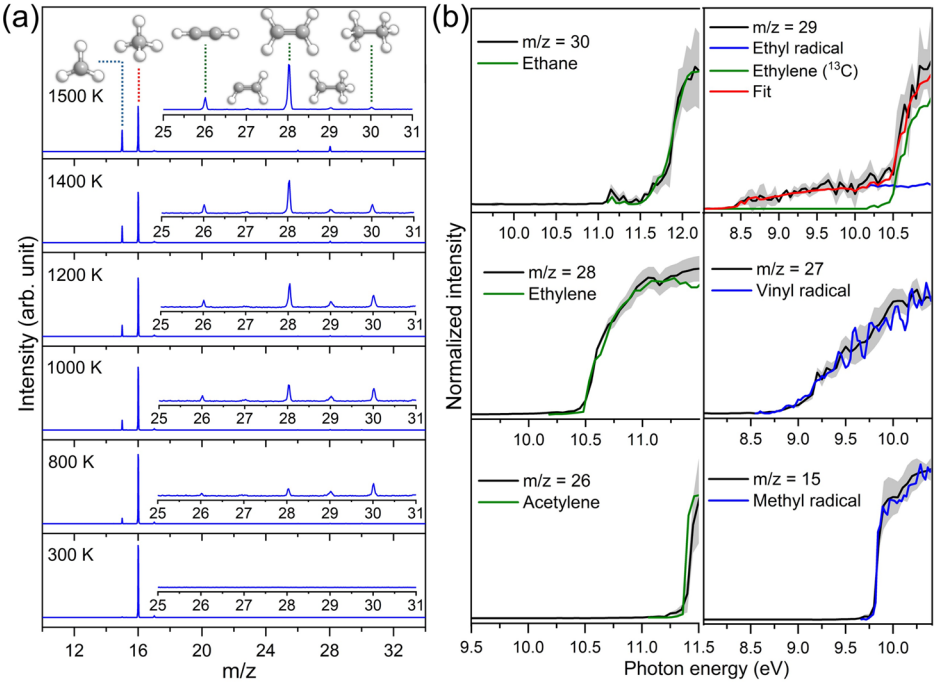

Figure 1. (a) Mass spectra recorded for the catalytic conversion of helium-seeded (2%) methane (CH_4) over titanium−aluminum−boron nanopowder (Ti−Al−B NP) in a high-temperature chemical microreactor at a photon energy of 13 eV in the 300 K to 1500 K range. The m/z = 25 to 31 segments in each spectrum are magnified 40 times to locate two-carbon mass-growth products. Negligible formation of C3 species can be seen in Figure S5. (b) Experimental photoionization efficiency curves (PIE, black traces) for the major catalytically formed products (C1 and C2 species) at distinct mass-to-charge ratios at 800 K. The experimental errors (gray shaded area) originate from the accuracy of the photocurrent measurement by the photodiode and a 1σ error of the PIE curves averaged over the individual scans. In case of multiple isomers, reference PIE curves are represented as blue and green traces; the overall fit is depicted in a red trace, whereas for a single species contributing to a mass peak, the reference trace is represented by the green or blue trace for closed-shell hydrocarbons or radicals, respectively.

Over the last few decades, multiple categorical NOCM catalysts have been exploited to increase the C2 hydrocarbon yield and selectivity. Zeolite-supported molybdenum catalysts exhibit C−C coupling activity but suffer from rapid deactivation due to coke formation[22] and do not provide dominant selectivity toward C2 hydrocarbons rather favor dehydroaromatization.[23−26] Iron single-site catalysts embedded in silica selectively form ethylene alongside competing yield of aromatics including benzene and naphthalene at temperatures above 1300 K, and the catalytic processes are limited by the absence of adjacent reactive sites.[17] Noble-metal-based catalysts, including Pt single sites on CeO_2 and Pt-based bimetallic (e.g., Pt−Bi) and trimetallic (e.g., Pt−Bi/Mo) systems, lower activation barriers and enhance selectivity but rely on scarce and costly elements and often demand structurally fragile zeolite supports (e.g., Pt−Bi/Mo/ZSM-5).[27−34] These scientific constraints serve as the impetus in developing a novel class of efficient, selective, and economically affordable heterogeneous catalyst which is not only resistant to coke formation but also exploits low-cost alternatives to expensive platinum group metals and operates at low temperatures. A critical yet often underappreciated challenge in NOCM is hydrogen management. Accumulation of adsorbed hydrogen promotes rapid recombination and methane reformation, whereas excessive hydrogen abstraction leads to deep dehydrogenation and coke formation.[35] Catalysts capable of reversibly storing and redistributing hydrogen during turnover could, in principle, decouple C−H activation from C−C coupling and enable selective formation of unsaturated C2 products such as ethylene, a particularly demanding benchmark for nonoxidative methane conversion. Methodologically, it is imperative to identify the initial products and intermediates, including radicals, which assess the true catalytic potential and reaction mechanism of a NOCM catalyst at the molecular level.

Here, we demonstrate that sonochemically synthesized, atomically dispersed titanium−aluminum−boron nanopowder (Ti−Al−B NP) constitutes a distinct class of heterogeneous catalyst that fulfills these above-mentioned criteria. By combining a catalytic microreactor (Figure S1) with synchrotron-based single-photon photoionization reflectron time-of-flight mass spectrometry (PI-ReTOF-MS), we directly probe nascent reaction products and radical intermediates formed during methane activation under nonoxidative conditions. This soft-ionization, in situ approach enables unambiguous identification of primary C2 hydrocarbons—ethane (C_2H_6), ethylene (C_2H_4), and acetylene (C_2H_2)—as well as key open-shell intermediates, providing molecular-level insight inaccessible to conventional analytical techniques.[36−40] In the presence of Ti−Al−B NP, the onset temperature for methane decomposition is reduced by 700 K, from 1500 K in the gas phase to 800 K, with ethylene emerging as the dominant C−C coupled product and reaching selectivity of up to 78%. Comprehensive electronic structure calculations on model Ti−Al−B clusters reveal a complex heterogeneous catalysis cycle involving molecular adsorption of two methane molecules with subsequent reaction, isomerization, and desorption, which starts with a facile Ti/B-mediated C−H bond rupture at 800 K with a barrier of only 38 kJ mol^{-1} (30 kJ mol^{-1} at 0 K). This process activates the C−H bond (439 kJ

https://doi.org/10.1021/jacs.6c01503
J. Am. Chem. Soc. 2026, 148, 10205−10215

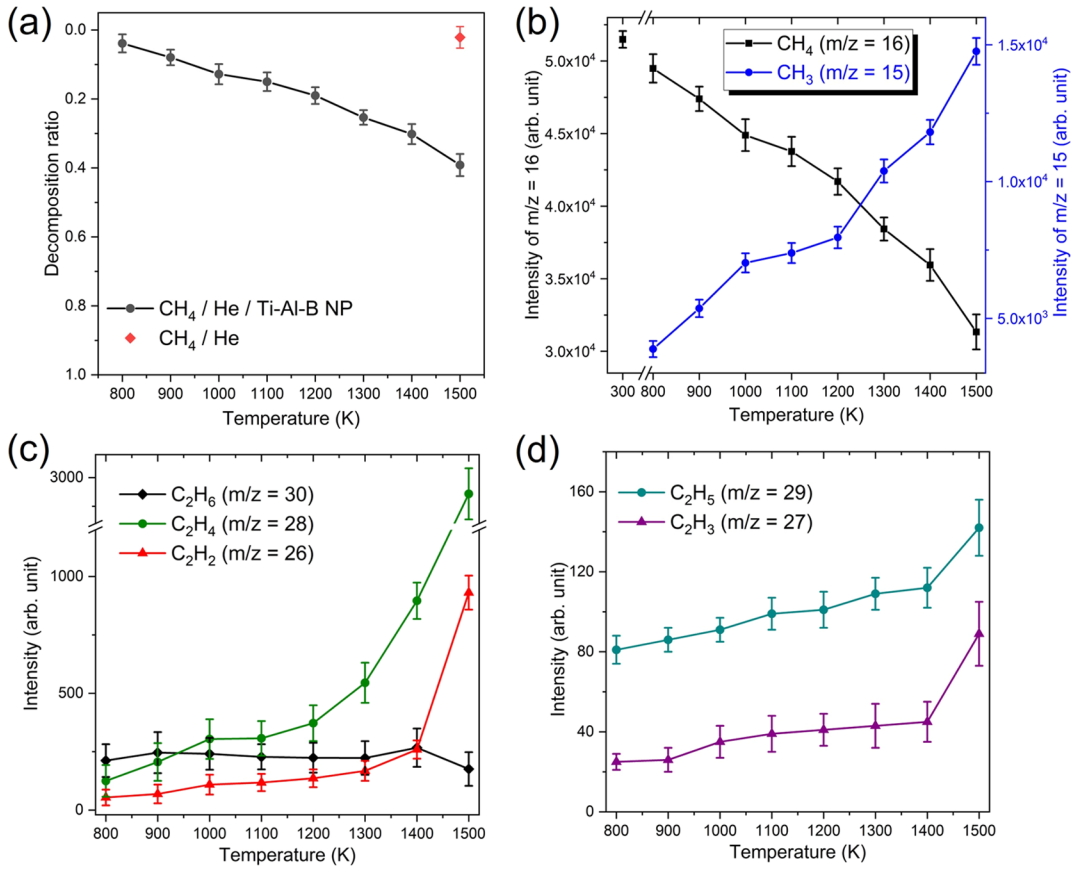

Figure 2. (a) Decomposition ratios of methane with and without Ti−Al−B NP catalyst loading. For the uncatalyzed reaction, decomposition of methane starts at 1500 K, indicated by a *red* diamond symbol. (b−d) Temperature-dependent relative abundances of methane and the C2 products (closed and open-shell hydrocarbons) from mass spectra recorded at 13 eV. The species are grouped as—(b) C1-species, (c) C2-closed-shell hydrocarbons, and (d) C2-radicals.

mol^{-1}) in methane, thus effectively competing with the catalytic potential of platinum in C−H activation with a barrier of 99 kJ mol^{-1}.[41] The molecular-level understanding exposed here is essential in deciphering the specific roles of distinct metals in this new class of heterogeneous hybrid catalysts: titanium serves as the exclusive docking center for methane adsorption, enabling C−H bond activation and mediating the catalytic C−C coupling process; boron functions as a hydrogen reservoir, storing the abstracted hydrogen atoms, while aluminum provides a suitable coordination environment that facilitates dehydrogenation steps and stabilizes the adsorbed methylene (CH_2) intermediate. The molecular-level understanding presented here provides general design principles for next-generation heterogeneous catalysts based on synergistic roles of readily available elements for methane upgrading and light-alkane conversion.

RESULTS AND DISCUSSION

Identification of Products and Intermediates

The catalytically formed nascent gas-phase products of methane over Ti−Al−B NPs in the chemical microreactor are identified in situ with single photon photoionization (PI) reflectron time-of-flight mass spectrometry (Re-TOF-MS) (Figures 1a and S2). The mass spectra are recorded at definite temperature intervals. At 300 K, only the parent mass peak at m/z = 16 (CH_4^+) and a weak feature of its ^{13}C counterpart at m/z = 17 ($^{13}CH_4^+$) are observed. The first thermal reaction of CH_4 in the presence of Ti−Al−B NP is revealed at 800 K through the detection of the methyl radical at m/z = 15 which is the primary tracer for C−H activation. Under uncatalyzed conditions, the reaction commences only at 1500 K under otherwise identical experimental parameters (Figure S3). Several two-carbon (C2) mass-growth products appear in the range of m/z = 26−30 corroborating the catalytic C−C coupling. A detailed analysis of distinct *isomer-selective* photoionization efficiency (PIE) curves of individual mass-to-charge (m/z) peaks provides a confirmatory identification of the products and intermediates formed in the molecular beam (Figures 1b and S4). Mass growth beyond C2 products is negligible with very weak peaks of C3 hydrocarbon products at levels of less than 0.1% (Figure S5).

At 800 K, the ethane (C_2H_6) peak at m/z = 30 represents the strongest among the mass-growth products, followed by ethylene (C_2H_4, m/z = 28) and acetylene (C_2H_2, m/z = 26). Open-shell intermediates such as ethyl ($^{\bullet}C_2H_5$, m/z = 29) and vinyl ($^{\bullet}C_2H_3$, m/z = 27) radicals are also evident. The identification of these radical intermediates represents a key advantage of PI-ReTOF-MS compared to traditional analytical techniques such as gas chromatography−mass spectrometry (GC−MS), which fail to identify key reaction intermediates.

With the rise in temperature above 900 K, ethylene (C_2H_4, m/z = 28) becomes the most intense feature among the mass-growth products until 1500 K (Figure S3). Complementary mass spectra at a photon energy of 15.4 eV also detect molecular hydrogen (H_2, m/z = 2), indicating simultaneous

https://doi.org/10.1021/jacs.6c01503
J. Am. Chem. Soc. 2026, 148, 10205−10215

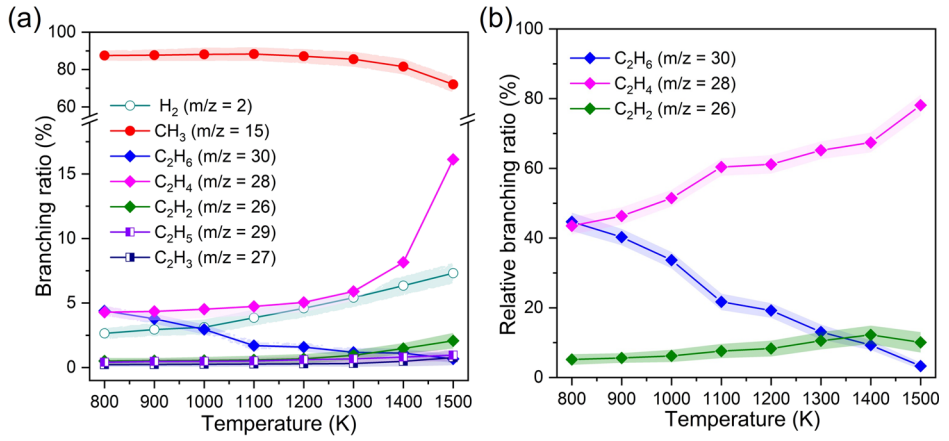

Figure 3. (a) Temperature-dependent overall branching ratios of individual products (C1 and C2 species) including molecular hydrogen. (b) Relative branching ratios of the major C2 products [ethane (C_2H_6), ethylene (C_2H_4), and acetylene (C_2H_2)] with respect to all the mass-growth products as a function of temperature. The error bars are evolved due to the uncertainties determined by averaging the recorded photoionization efficiency curves and respective integral peak areas from mass spectra.

catalytic dehydrogenation processes (Figure S6). It is important to note that repeated heating−cooling−heating cycles performed with the same catalyst (Experimental Methods, Supporting Information) produced no observable changes in the recorded mass spectra, indicating preserved chemical activity and an excellent catalyst lifecycle.

Decomposition Ratio and Temperature Profiles of the Key Products

To evaluate the temperature-dependent catalytic decomposition and reformation of methane and assess the performance of the Ti−Al−B nanopowder catalyst, the decomposition ratios of methane measured at distinct temperatures with and without catalyst loading are shown in Figure 2a. Here, the decomposition ratio or the *conversion fraction* is defined as the ratio of the decomposed methane to the total amount, where zero indicates no reaction, and the full consumption of the hydrocarbon is represented as unity. Experimentally, this ratio at a particular temperature is evaluated by probing the fractions of normalized parent mass peak intensities at m/z = 16 with respect to that observed at 300 K. From the plot, it is evident that in the presence of Ti−Al−B NP, the decomposition of methane (black circles) is initiated at a significantly lower temperature of 800 K, which is 700 K below the onset temperature of decomposition reaction in the absence of the catalyst (red diamond). At the maximum temperature of the study, i.e., 1500 K, the catalytic decomposition value or *methane conversion fraction* reaches 0.39 ± 0.03.

The gradual enhancement of the catalytic decomposition of methane with respect to the rising temperature is accompanied by a simultaneous increase in the C2 species (Figure 2b−d). The trend depicts that the yield of the primary product, the methyl radical ($^{\bullet}CH_3$, m/z = 15), continues to increase, while its recombination product ethane (C_2H_6) exhibits a nearly constant intensity with only a slow decay above 900 K. Most importantly, mass peak intensities for ethylene (C_2H_4, m/z = 28) rise sharply with temperature, indicating a preferential formation. Acetylene (C_2H_2, m/z = 26), on the other hand, maintains a steady growth until 1300 K, above which a pronounced increase in its mass peak intensity is observed. Radical intermediates such as ethyl ($^{\bullet}C_2H_5$, m/z = 29) and vinyl ($^{\bullet}C_2H_3$, m/z = 27) display a steady rise until 1400 K, followed by a jump at 1500 K. To quantify changes in product distribution as a function of temperature, product branching ratios are evaluated.

Product Branching Ratios

The individual branching ratios for the catalytically formed major products over the temperature range of 800−1500 K (Figures 3, S7, S8) provide a quantitative overview of the corresponding product mole fractions.[39,40] The branching ratio of the primary decomposition product—methyl ($^{\bullet}CH_3$) radical—is lowered from 87.5 ± 2.8% at 800 K to 72.1 ± 4.3% at 1500 K. Although branching ratios for ethane (C_2H_6, 4.4 ± 0.4%) and ethylene (C_2H_4, 4.3 ± 0.7%) appear similar at 800 K, the latter turns out to be the major C−C coupled product at and above 900 K and reaches 16.1 ± 0.8% at 1500 K. Notably, among all the mass growth products, ethylene reaches a relative branching ratio of 78% at 1500 K (Figure 3b). On the flipside, a significant decline in the ethane is noted with the rise in temperature, determined to be only 0.7 ± 0.3% at 1500 K. Formation of acetylene at low temperatures (800−1300 K) remains less than 1% and rises to 2.1 ± 0.6% at 1500 K. Favorable dehydrogenation by the Ti−Al−B NP catalyst is reflected through the production of molecular hydrogen (H_2) even at low-temperature ranges accounting for 2.6 ± 0.5% at 800 K. With the rise in temperature and increasing unsaturation in the C−C coupled products, branching ratio for molecular hydrogen also increased to 7.3 ± 0.8% at 1500 K. Ethyl ($^{\bullet}C_2H_5$, m/z = 29) and vinyl ($^{\bullet}C_2H_3$, m/z = 27) radicals are found to be minor products with individual branching ratios less than 1% within the entire experimental temperature range, while C3 products appear negligible and their total branching ratios remain less than 0.1% (Figure S9).

Reaction Mechanism of C−C Coupling

To decipher the mechanistic paths for the catalytic activity of Ti−Al−B NPs in the low-temperature nonoxidative C−C coupling of methane, we computationally explored the role of model Ti−Al−B clusters. Previously, we reported structural details of the model cluster based on the extensive characterization, e.g., high-angle annular dark-field scanning transmission electron microscopy (HAADF-STEM) with complementary electron energy loss spectroscopy (EELS) and energy-dispersive X-ray spectroscopy (EDS), nuclear magnetic resonance (NMR), Raman, and X-ray photoelectron spectroscopy (XPS) of the material.[36] Average particle diameter of the

https://doi.org/10.1021/jacs.6c01503
J. Am. Chem. Soc. 2026, 148, 10205−10215

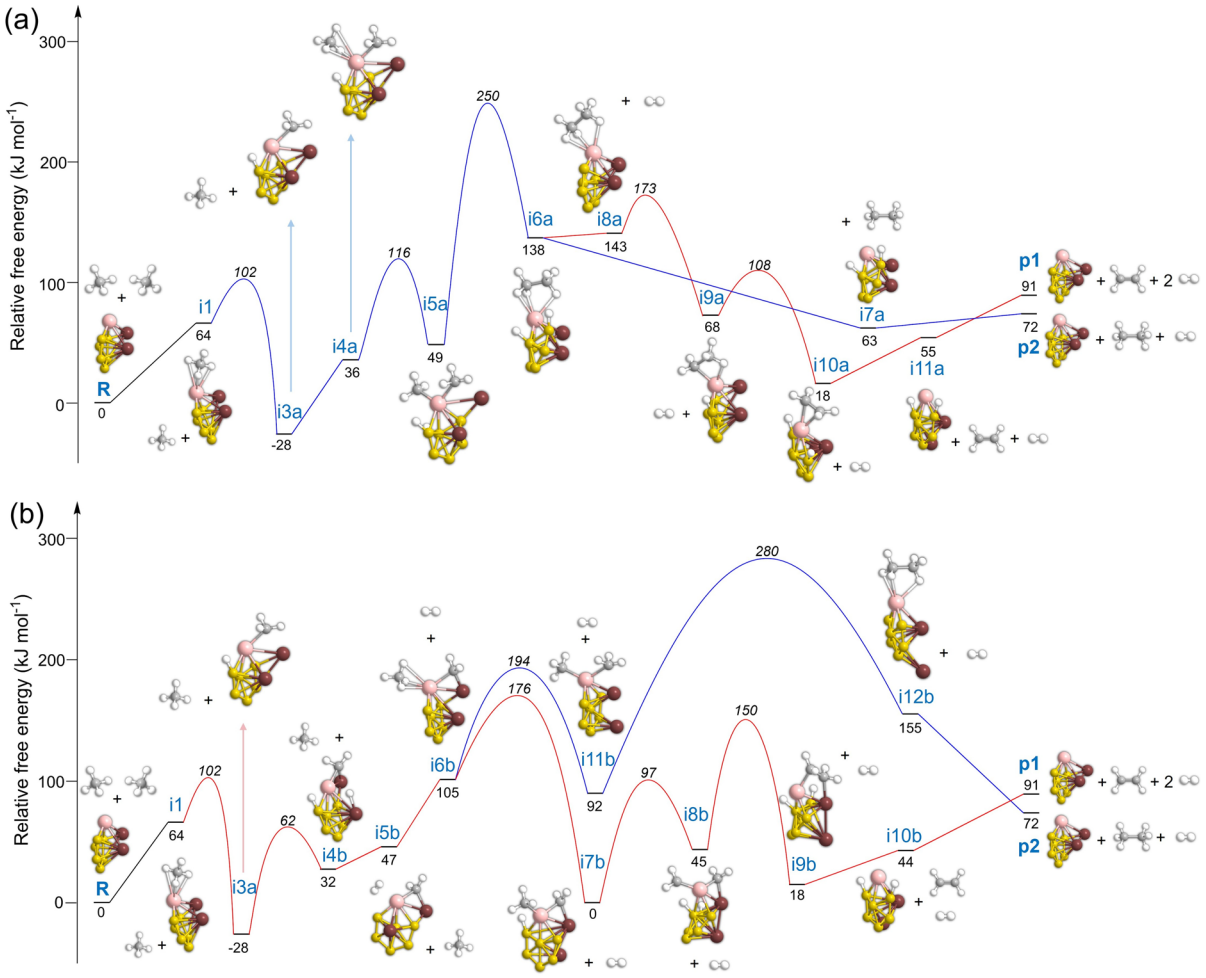

Figure 4. Free-energy surfaces for the formation of ethylene (C_2H_4) and ethane (C_2H_6) via the global minimum (**i1**) of the methane−$TiAl_2B_6$ binding complex at 800 K. The second methane gets adsorbed, while the (a) methyl (CH_3) or (b) methylene (CH_2) group is attached on the Ti center.

nanopowder revealed by dynamic light scattering (DLS) is measured to be 448 nm with a narrow size distribution (standard deviation of 10.8 nm).[42] The predominant presence of elemental states of the atomic constituents with heteroatomic interactions and linkages such as Ti−B, Al−B, and Ti−Al moieties was revealed along with extensive spatial atomic dispersion. Hence, the chemically simplest cluster ($TiAl_2B_6$) of the correct stoichiometry as determined by inductively coupled plasma optical emission spectroscopy (ICP−OES)[42,43] was theoretically modeled using a stochastic structure search (global optimization). It is important to note that no alloy of this composition exists that would permit modeling the catalyst as faceted nanoparticles; consequently, the particles are most appropriately represented by clusters of matching stoichiometry, a methodology well established in the catalysis literature.[44−48]

In detail, the global minimum identified from approximately 700 initial structures of the $TiAl_2B_6$ cluster is selected for subsequent computations (Supporting Information, Computational Methods). From a chemical perspective, the onset temperature of the catalytic reaction, 800 K, is used as the primary reaction temperature, with calculations extended to 1500 K for comparison. The initial binding interaction between methane and the $TiAl_2B_6$ cluster is taken to represent the substrate adsorption on the catalyst surface. For such alkanes-on-cluster catalysts, it is rather typical to proceed directly to chemisorption while not showing a physisorbed well on the free-energy surface.[49] Binding complexes involving the $TiAl_2B_6$ cluster are simulated with a tight SCF convergence using the BLYP functional[50,51] with the def2-TZVP basis set[52] and def2/J auxiliary basis set.[53] Dispersion interactions are accounted for using the D3BJ correction.[54,55] These computations yield two major low energy geometries (Figure S10) which are stabilized by approximately 38 kJ mol^{-1} at 0 K with respect to the separated reactants, and their Boltzmann populations at 800 K are evaluated to be 55 and 45%, respectively. In both initial binding complexes, methane gets symmetrically docked to the Ti center of the cluster via the formation of three C−H−Ti linkages.

The reaction mechanisms of the catalytic NOCM are investigated by the electronic structure theory calculation involving the model cluster and two molecules of methane ($TiAl_2B_6$ + 2 CH_4; **R**), where their combined energy has been considered as the reference, i.e., 0 kJ mol^{-1}. The computation of the free-energy surfaces (FESs) constructed via the Nudged Elastic Band (NEB) method[56,57] with vibrational, translational, and rotational entropy corrections reveals that simultaneous adsorption of two methane molecules on $TiAl_2B_6$ is entropically unfavored at experimental temperatures, resulting in a high-energy intermediate, 130 kJ mol^{-1} at 800 K, rather the

https://doi.org/10.1021/jacs.6c01503
J. Am. Chem. Soc. 2026, 148, 10205−10215

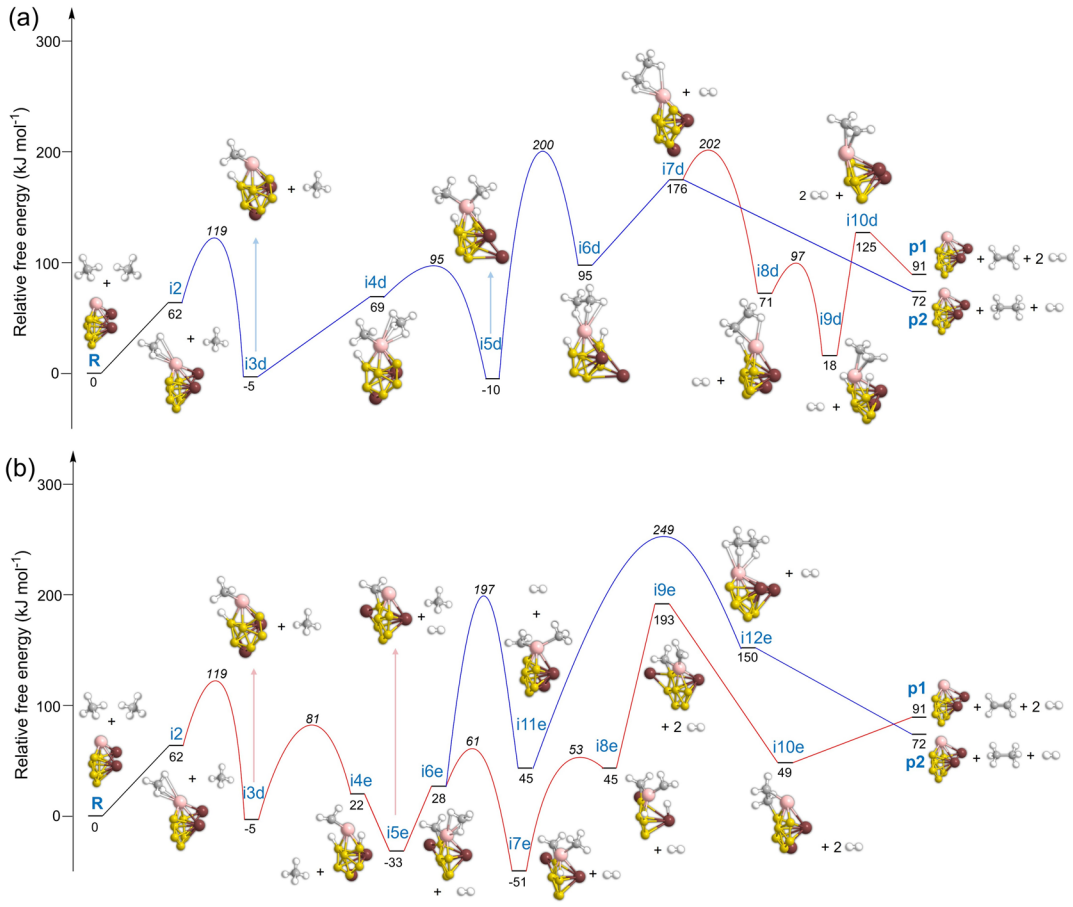

Figure 5. Free-energy surfaces for the formation of ethylene (C_2H_4) and ethane (C_2H_6) via the first local minimum (**i2**) of the methane−$TiAl_2B_6$ binding complex at 800 K. The second methane gets adsorbed, while the (a) methyl (CH_3) or (b) methylene (CH_2) group is attached on the Ti center.

reactions proceed through sequential methane adsorption (Figures 4−6, S11, and S12). The FES is further developed from the global minimum (**i1**) and the first local minimum (**i2**) of the $TiAl_2B_6$−CH_4 complexes. Depending on the stage at which the second methane molecule is introduced, minimum energy reaction pathways are identified and analyzed using entropy-corrected free-energy profiles. Notably, the barrier for the initial C−H bond cleavage via **i1** → **i3a** or **i2** → **i3d** is reduced to approximately 30 and 45 kJ mol^{-1}, respectively, at 0 K (Tables S1 and S4), compared to about 440 kJ mol^{-1} for homolytic methane cleavage in the gas phase.[4]

Ethylene and Ethane Formation Pathways

The entrance channel corresponding to adsorption of the first methane molecule, forming the CH_4···$TiAl_2B_6$ complex (**i1**), represents the global minimum of 1:1 binding configuration. At 800 K, this adsorption step is entropically unfavorable, resulting in an increase of the free energy of **i1** to 64 kJ mol^{-1} relative to −38 kJ mol^{-1} at 0 K, yet it remains accessible at elevated temperature (Figure 4). From **i1**, a titanium-mediated hydrogen atom transfer occurs to an adjacent boron center located at the periphery of the B_5 moiety and opposite the distal or exterior aluminum atom via proceeding intermediate **i3a** with an associated barrier of 38 kJ mol^{-1}. Subsequent adsorption of the second methane molecule at the titanium center yields intermediate **i4a** at 56 kJ mol^{-1}, followed by hydrogen atom transfer to the central boron atom through a barrier of 80 kJ mol^{-1} to form **i5a**. The transition from **i5a** → **i6a** constitutes the key C−C coupling step between the two adsorbed methyl groups, crossing a barrier of 201 kJ mol^{-1} to generate adsorbed ethane on the $H_2TiAl_2B_6$ cluster. This C−C coupling step corresponds to the highest transition state energy on the FES, reaching 250 kJ mol^{-1}. The catalytic cycle leading to ethane formation (**R** → **p2**) is concluded by the successive desorption of ethane (**i7a**) and molecular hydrogen (H_2).

Alternatively, the C_2H_6−$H_2TiAl_2B_6$ complex (**i6a**) can undergo molecular hydrogen desorption to form **i8a**, followed by successive hydrogen atom transfer steps with barriers of 30 and 40 kJ mol^{-1}, respectively, leading to the formation of bound ethylene (**i10a**). In this intermediate, the C_2H_4 molecule adopts a slightly nonplanar geometry, with the hydrogen atoms oriented upward relative to the $H_2TiAl_2B_6$ cluster. The $TiAl_2B_6$ cluster is regenerated (**p1**) upon the successive desorption of ethylene (**i11a**) and molecular hydrogen. Formation of both the C−C coupled products **p1** (C_2H_4 + 2 H_2) and **p2** (C_2H_6 + H_2) is endoergic by 91 and 72 kJ mol^{-1}, respectively, at 800 K.

Instead of accommodating the second methane molecule on **i3a**, subsequent H atom transfer can form the chemisorbed methylene group (**i4b**) via crossing a barrier of 90 kJ mol^{-1} (Figure 4b). Further, molecular hydrogen (H_2) desorption via **i5b** allows the adsorption of the second methane (**i6b**), which eventually undergoes successive H atom transfers (**i6b** → **i7b** → **i8b**) forming two adsorbed methylene groups—those undergo C−C coupling via an energy barrier of 105 kJ mol^{-1} to generate the adsorbed C_2H_4 moiety (**i9b**). Next, the

https://doi.org/10.1021/jacs.6c01503
J. Am. Chem. Soc. 2026, 148, 10205−10215

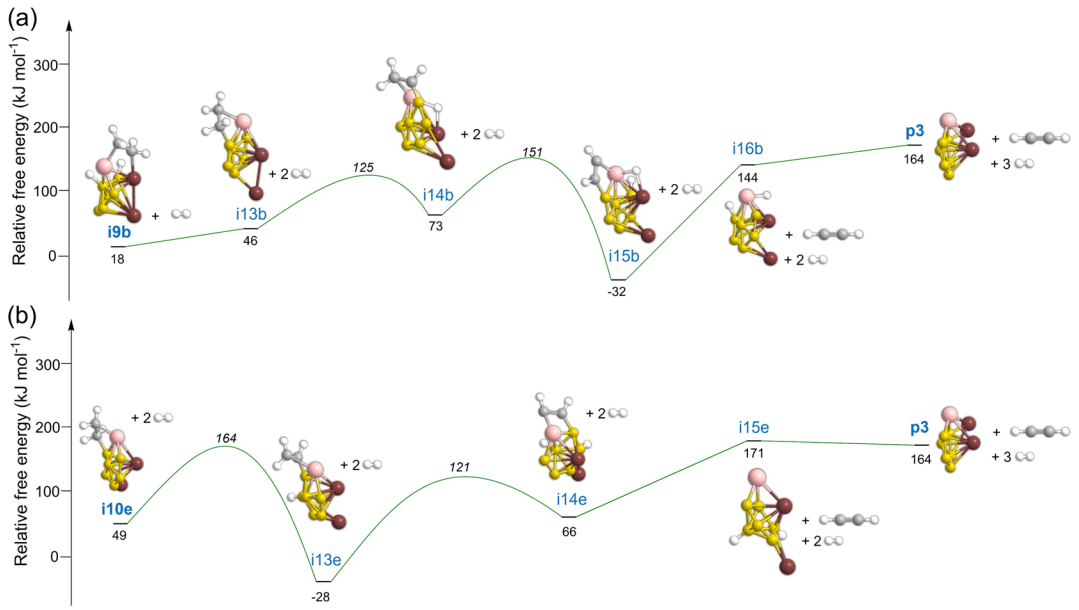

Figure 6. Representative free-energy surfaces for the formation of acetylene (C_2H_2) via the (a) global minimum (**i1**) and the (b) first local minimum (**i2**) of the methane−$TiAl_2B_6$ binding complex at 800 K, extended from the selected pathways in Figures 4 and 5.

desorption steps of ethylene and the remaining molecular hydrogen (H_2) complete the catalytic cycle attaining **p1**. At **i6b**, a H atom transfer from the adsorbed methane to the methylene moiety can generate two methyl groups (**i11b**) which upon C−C coupling via a barrier of 188 kJ mol^{-1} produces adsorbed ethane (**i12b**) that ultimately leads to **p2** through desorption. Notably, among the four pathways originating from the global minimum structure (**i1**) and presented in Figure 4, the ethylene formation pathway proceeding through initial methylenated intermediate **i4b** is energetically most favorable. In this case, it has the smallest energetic span[58] and the highest transition state lies at 176 kJ mol^{-1} relative to the separated reactants, compared to barriers of at least 250 kJ mol^{-1} for ethane formation. In addition, an alternative ethylene formation pathway involving methylene−methylene C−C coupling is identified, with a maximum barrier of 207 kJ mol^{-1} (Figure S11).

A similar trend is also observed for the pathways of ethylene and ethane generation involving the first local minimum of the methane−$TiAl_2B_6$ complex (**i2**, 62 kJ mol^{-1}). Comparison of the two possible pathways for each product, either through direct methyl−methyl coupling (Figure 5a) or via a methylenated intermediate (Figure 5b), indicates that the latter is energetically favored, consistent with the observed higher yield of ethylene. Briefly, the direct methyl−methyl C−C coupling step (**i5d** → **i6d**) proceeds via the highest energy TS of 200 kJ mol^{-1} for the ethane channel. Within the same FES, dehydrogenation of the adsorbed ethane intermediate (**i7d** → **i8d**) includes a TS at 202 kJ mol^{-1} along the pathway leading to ethylene formation. In contrast, the dehydrogenated, methylenated intermediate (**i5e**) undergoes successive methane adsorption (**i6e**), dehydrogenation steps (**i7e**, **i8e**), and desorption (**i9e**), ultimately yielding two methylene groups adsorbed at the titanium center. The **i9e** intermediate essentially undergoes barrierless C−C coupling, forming an adsorbed C_2H_4 moiety (**i10e**), followed by desorption of an ethylene molecule (**p1**) desorption. Along the **R** → **i6e** → **i9e** → **p1** pathway, the highest energy point encountered is at 193 kJ mol^{-1} (**i9e**). In contrast, the formation of ethane from the **i6e** intermediate requires higher energy transition states associated with H atom transfer (197 kJ mol^{-1}) and C−C coupling (249 kJ mol^{-1}), rendering this pathway less favorable than the ethylene formation pathways described above. An alternate pathway involving a methylenated intermediate is shown in Figure S12a, where the initial H atom transfer occurs to the central boron atom (**i3f**).

Acetylene Formation Pathways

Representative acetylene formation pathways (Figures 6, S12b, and S13) are found by extending selected FES that produce ethylene via global (**i1**) or the first local minimum (**i2**) of the methane−$TiAl_2B_6$ complex. Intermediate **i9b** (Figures 4b and 6a) upon hydrogen desorption forms C_2H_4···$TiAl_2B_6$ (**i13b**), which further undergoes H atom transfers and desorption steps to yield acetylene (**p3**). The highest energy TS in this path (**i9b** → **p3**) is noted at 151 kJ mol^{-1}, designating H atom transfer from the adsorbed vinylic (C_2H_3) moiety to the distal B atom. However, with respect to the separated reactants, the acetylene formation path is found to be endoergic by 164 kJ mol^{-1} at 800 K which is substantially higher than ethylene (91 kJ mol^{-1}) or ethane (72 kJ mol^{-1}) corroborating its negligible yield observed at this temperature. Similarly, the intermediate **i10e** (Figures 5b and 6b) originating from the **i2** binding configuration can undergo successive H atom transfers (**i10e** → **i13e** → **i14e**), followed by sequential desorption events (**i14e** → **i15e** → **p3**) to yield acetylene. In both pathways shown in Figure 6, acetylene desorption is associated with high endoergicities of 176 (**i15b** → **i16b**) and 105 kJ mol^{-1} (**i14e** → **i15e**), respectively. It is to be noted here that the cluster geometries become highly distorted during the third dehydrogenation steps to accommodate the acetylenic moiety, thus adopting nonidentical metastable energy minima (e.g., **i16b** versus **i15e**) along the reaction path.

Open-Shell Products

The methyl radical ($^{\bullet}CH_3$), the most abundant species formed aside from C2 products and a key tracer for the C−H activation, can be generated from intermediates in which two methyl groups are simultaneously adsorbed at the Ti atom

https://doi.org/10.1021/jacs.6c01503
J. Am. Chem. Soc. 2026, 148, 10205−10215

prior to the C−C coupling. The pathways shown in Figures S14 and S15 show that two methyl radicals are successively desorbed through entropically favorable yet endoergic pathways from key intermediates such as **i5a**, **i11b**, **i5d**, and **i11e**. Because each catalytic cycle of the $TiAl_2B_6$ cluster stoichiometrically releases one unit of molecular hydrogen and two methyl radicals, the comparatively large branching ratio of the methyl radical is readily rationalized. Minor open-shell products, including ethyl and vinyl radicals, can plausibly be desorbed from appropriate intermediates such as **i9a** and **i14b** through endoergic pathways.

Temperature Effects on the Free Energy Surfaces (FESs)

To assess the temperature dependence on the pathways leading to ethylene, ethane, and acetylene, the corresponding free-energy profiles are also computed at 1500 K (Tables S1−S6). The increase in temperature leads to pronounced changes in the FES, most notably a reduction in reaction endoergicity. For example, the endoergicity of the ethane formation pathway decreases to 56 kJ mol^{-1} at 1500 K, compared to 72 kJ mol^{-1} at 800 K. However, the reaction channels for the formation of ethylene and acetylene eventually become exoergic (−18 and −40 kJ mol^{-1}) at 1500 K which corroborates the experimentally observed increase in the yields of these two products. For ethylene, the relative branching ratio among the mass growth products increases from 43.5 ± 2.5% at 800 K to 78.1 ± 2.9% at 1500 K. Consistent with this trend, the computed FESs indicate that nearly all desorption steps become energetically downhill at 1500 K, thereby facilitating product exit channels. Although dehydrogenation barriers increase upon inclusion of temperature corrections, the substantially greater thermal energy at 1500 K enables a much larger fraction of reactants to access the corresponding transition states. For example, in the dehydrogenation step **i1** → **i3a**, only approximately 0.3% of the reactant population (**i1**) can overcome the energy barrier at 800 K based on Boltzmann statistics, whereas this fraction increases to about 2% at 1500 K. Enhanced dehydrogenations at elevated temperature are further reflected in the pronounced decrease in the evaluated relative branching ratio of ethane among all mass growth products, from 44.7 ± 2.6% at 800 K to 3.3 ± 0.9% at 1500 K.

Taken together, the computational results reveal a clear functional differentiation among the constituent elements of the Ti−Al−B model cluster. The titanium center serves exclusively as the docking site for both methane molecules and forms Ti−C bonds that stabilize hydrocarbon fragments, such as methyl and methylene groups, in key catalytic intermediates. This behavior is reminiscent of alkene polymerization on titanium-based Ziegler−Natta catalysts in higher oxidation states, where initiation and propagation proceed through Ti−C bond formation involving inserted hydrocarbon species.[59] The boron atoms within the B_6 framework act as reversible hydrogen storage sites, accommodating stepwise hydrogen atom transfers from methane and adsorbed hydrocarbon intermediates and thereby regulating hydrogen availability during the catalytic cycle.[59,60] In contrast, the aluminum atoms, particularly the exterior Al site, exhibit pronounced fluxionality along the free-energy surfaces, creating a transient coordination space for hydrogen atoms generated during dehydrogenation. In addition, aluminum contributes to stabilizing methylene intermediates through direct coordination, facilitating selective C−C coupling and dehydrogenation. While this fluxional behavior may be amplified in the small cluster model, it is expected to persist, albeit in a moderate form, in larger nanoparticle ensembles.

CONCLUSIONS

In summary, we have demonstrated a low-temperature nonoxidative coupling of methane on an atomically dispersed titanium−aluminum−boron (Ti−Al−B) catalyst at 800 K that enables controlled C−H activation and facile C−C bond formation at temperatures substantially lower than those required in the gas phase. By combining operando, isomer selective synchrotron photoionization mass spectrometry in a chemical microreactor coupled with electronic structure calculations, we directly identify nascent reaction products including radical intermediates and elucidate the elementary steps governing methane activation, C−C coupling, and dehydrogenation under nonoxidative conditions. Further, temperature-varied experimental runs precisely map the reactivity as well as functionality of the Ti−Al−B nanopowder over a broad temperature range, where ethylene emerges as the most contributing C2 product with the rise in temperature along with elevated molecular hydrogen release, corroborating facile dehydrogenation on the catalyst. Extensive electronic structure theory calculations recognize a cooperative catalytic mechanism in which chemically differentiated elements perform distinct and complementary functions. Titanium serves as the primary adsorption and activation site for methane and mediates C−C bond formation; boron acts as a reversible hydrogen reservoir that stabilizes abstracted hydrogen atoms and regulates hydrogen availability during turnover, and aluminum stabilizes dehydrogenated methylene intermediates while facilitating selective dehydrogenation that promotes ethylene selectivity. The orchestrated abilities of the Ti−Al−B nanopowder within a single catalytic ensemble therefore establish a distinct catalyst architecture for nonoxidative methane conversion. Moreover, this efficient multimetal catalyst, built from earth-abundant elements, offers a low-cost alternative to platinum and other noble metals. Its experimentally and computationally validated C−H activation and dehydrogenation capabilities make Ti−Al−B nanopowder a promising candidate for advanced hydrocarbon-reforming reactions, including propane dehydrogenation and ethylene aromatization.

ASSOCIATED CONTENT

Data Availability Statement

The data that support the findings of this study are available from the corresponding author upon reasonable request.

Supporting Information

The Supporting Information is available free of charge at https://pubs.acs.org/doi/10.1021/jacs.6c01503.

Experimental and computational methods; schematic of catalytic microreactor-coupled molecular beam machine; mass spectra at 13 eV in the 300 to 1500 K range with 100 K interval; comparison of mass spectra for the products with and without catalyst; photoionization efficiency curves of the major products at 1500 K; comparison of mass spectra (m/z = 20−60) at 800 and 1500 K; mass spectra at 15.4 eV for representative temperatures; stack plot of branching ratios of major products at different temperatures; temperature-dependent individual branching ratios of closed-shell hydro-

https://doi.org/10.1021/jacs.6c01503
J. Am. Chem. Soc. 2026, 148, 10205−10215

carbons and radicals at different temperatures; temperature-dependent individual branching ratios of C3 species; global and first local minima of the methane−$TiAl_2B_6$ complexes; additional free energy surfaces for the formation of ethylene via the global minimum of the methane−$TiAl_2B_6$ binding complex at 800 K; additional FES for the formation of ethylene, ethane, and acetylene via the first local minimum at 800 K; FES for the formation of acetylene extended from Figure 4a; FES for methyl desorption via the global minimum at 800 K; FES for methyl desorption via the first local minimum at 800 K; tables containing relative energies corresponding to free-energy profiles at 0, 800, and 1500 K; and coordinates of the intermediates, transition states, reactants, and products (PDF)

AUTHOR INFORMATION

Corresponding Authors

Albert Epshteyn − *Chemistry Division, U.S. Naval Research Laboratory, Washington, District of Columbia 20375, United States;* orcid.org/0000-0002-4489-2296; Email: albert.epshteyn.civ@us.navy.mil

Anastassia N. Alexandrova − *Department of Chemistry and Biochemistry, University of California, Los Angeles, Los Angeles, California 90095, United States;* orcid.org/0000-0002-3003-1911; Email: ana@chem.ucla.edu

Musahid Ahmed − *Chemical Sciences Division, Lawrence Berkeley National Laboratory, Berkeley, California 94720, United States;* orcid.org/0000-0003-1216-673X; Email: mahmed@lbl.gov

Ralf I. Kaiser − *Department of Chemistry, University of Hawai'i at Manoa, Honolulu, Hawaii 96822, United States;* orcid.org/0000-0002-7233-7206; Email: ralfk@hawaii.edu

Authors

Souvick Biswas − *Department of Chemistry, University of Hawai'i at Manoa, Honolulu, Hawaii 96822, United States;* orcid.org/0000-0002-1643-2663

Avital Isakov − *Department of Chemistry and Biochemistry, University of California, Los Angeles, Los Angeles, California 90095, United States*

Nureshan Dias − *Chemical Sciences Division, Lawrence Berkeley National Laboratory, Berkeley, California 94720, United States;* orcid.org/0000-0002-4518-0901

Matthew T. Finn − *Chemistry Division, U.S. Naval Research Laboratory, Washington, District of Columbia 20375, United States;* orcid.org/0000-0001-9474-7022

Jack Cokas − *Department of Chemistry and Biochemistry, University of California, Los Angeles, Los Angeles, California 90095, United States*

Complete contact information is available at: https://pubs.acs.org/10.1021/jacs.6c01503

Notes

The authors declare no competing financial interest.

ACKNOWLEDGMENTS

The Hawaii group is supported by the United States Office of Naval Research (ONR) under Contract Number N00014-22-1-2010. UCLA research is sponsored by the Air Force Office of Scientific Research grant AFOSR FA9550-22-1-0381. This work used computational and storage services associated with the DOD HPC, National Energy Research Scientific Computing Center, which is supported by the Office of Science of the U.S. Department of Energy under Contract No. DE-AC02-05CH11231, and UCLA IDRE Shared Cluster Hoffman2. M.A. and N.D. are supported by the Director, Office of Science, Office of Basic Energy Sciences, of the U.S. Department of Energy under Contract No. DE-AC02-05CH11231, through the Gas Phase Chemical Physics program of the Chemical Sciences Division. This research used resources of the Advanced Light Source, a U.S. DOE Office of Science User Facility under contract no. DE-AC02-05CH11231.

REFERENCES

(1) McFarland, E. Unconventional Chemistry for Unconventional Natural Gas. *Science* **2012**, *338*, 340−342.

(2) Kondratenko, E. V.; Peppel, T.; Seeburg, D.; Kondratenko, V. A.; Kalevaru, N.; Martin, A.; Wohlrab, S. Methane Conversion into Different Hydrocarbons or Oxygenates: Current Status and Future Perspectives in Catalyst Development and Reactor Operation. *Catal. Sci. Technol.* **2017**, *7*, 366−381.

(3) Schwach, P.; Pan, X.; Bao, X. Direct Conversion of Methane to Value-Added Chemicals over Heterogeneous Catalysts: Challenges and Prospects. *Chem. Rev.* **2017**, *117*, 8497−8520.

(4) Tomkins, P.; Ranocchiari, M.; van Bokhoven, J. A. Direct Conversion of Methane to Methanol under Mild Conditions over Cu-Zeolites and beyond. *Acc. Chem. Res.* **2017**, *50*, 418−425.

(5) Tang, P.; Zhu, Q.; Wu, Z.; Ma, D. Methane Activation: The Past and Future. *Energy Environ. Sci.* **2014**, *7*, 2580−2591.

(6) Xie, J.; Jin, R.; Li, A.; Bi, Y.; Ruan, Q.; Deng, Y.; Zhang, Y.; Yao, S.; Sankar, G.; Ma, D.; Tang, J. Highly Selective Oxidation of Methane to Methanol at Ambient Conditions by Titanium Dioxide-Supported Iron Species. *Nat. Catal.* **2018**, *1*, 889−896.

(7) Farrell, B. L.; Igenegbai, V. O.; Linic, S. A Viewpoint on Direct Methane Conversion to Ethane and Ethylene Using Oxidative Coupling on Solid Catalysts. *ACS Catal.* **2016**, *6*, 4340−4346.

(8) Paréja, P.; Mercy, M.; Gachon, J.-C.; Amariglio, A.; Amariglio, H. A Way to Higher Hydrocarbons from Methane with Sizable Yield and Good Selectivity. *Ind. Eng. Chem. Res.* **1999**, *38*, 1163−1165.

(9) Huang, K.; Miller, J. B.; Huber, G. W.; Dumesic, J. A.; Maravelias, C. T. A General Framework for the Evaluation of Direct Nonoxidative Methane Conversion Strategies. *Joule* **2018**, *2*, 349−365.

(10) Choudhary, T. V.; Aksoylu, E.; Wayne Goodman, D. Nonoxidative Activation of Methane. *Catal. Rev.-Sci. Eng.* **2003**, *45*, 151−203.

(11) Soulivong, D.; Norsic, S.; Taoufik, M.; Coperet, C.; Thivolle-Cazat, J.; Chakka, S.; Basset, J.-M. Non-Oxidative Coupling Reaction of Methane to Ethane and Hydrogen Catalyzed by the Silica-Supported Tantalum Hydride: (≡SiO)2Ta−H. *J. Am. Chem. Soc.* **2008**, *130*, 5044−5045.

(12) Zhang, P.; Li, J.; Huang, H.; Sui, X.; Zeng, H.; Lu, H.; Wang, Y.; Jia, Y.; Steele, J. A.; Ao, Y.; Roeffaers, M. B. J.; Dai, S.; Zhang, Z.; Wang, L.; Fu, X.; Long, J. Platinum Single-Atom Nests Boost Solar-Driven Photocatalytic Non-Oxidative Coupling of Methane to Ethane. *J. Am. Chem. Soc.* **2024**, *146*, 24150−24157.

(13) Ma, Y.; Han, X.; Xu, S.; Li, Z.; Lu, W.; An, B.; Lee, D.; Chansai, S.; Sheveleva, A. M.; Wang, Z.; Chen, Y.; Li, J.; Li, W.; Cai, R.; da Silva, I.; Cheng, Y.; Daemen, L. L.; Tuna, F.; McInnes, E. J. L.; Hughes, L.; Manuel, P.; Ramirez-Cuesta, A. J.; Haigh, S. J.; Hardacre, C.; Schröder, M.; Yang, S. Direct Conversion of Methane to Ethylene and Acetylene over an Iron-Based Metal−Organic Framework. *J. Am. Chem. Soc.* **2023**, *145*, 20792−20800.

(14) Belgued, M.; Pareja, P.; Amariglio, A.; Amariglio, H. Conversion of Methane into Higher Hydrocarbons on Platinum. *Nature* **1991**, *352*, 789−790.

(15) Li, Z.; Xiao, Y.; Chowdhury, P. R.; Wu, Z.; Ma, T.; Chen, J. Z.; Wan, G.; Kim, T.-H.; Jing, D.; He, P.; Potdar, P. J.; Zhou, L.; Zeng, Z.; Ruan, X.; Miller, J. T.; Greeley, J. P.; Wu, Y.; Varma, A. Direct Methane Activation by Atomically Thin Platinum Nanolayers on Two-Dimensional Metal Carbides. *Nat. Catal.* **2021**, *4*, 882−891.
(16) Dipu, A. L.; Ohbuchi, S.; Nishikawa, Y.; Iguchi, S.; Ogihara, H.; Yamanaka, I. Direct Nonoxidative Conversion of Methane to Higher Hydrocarbons over Silica-Supported Nickel Phosphide Catalyst. *ACS Catal.* **2020**, *10*, 375−379.
(17) Guo, X.; Fang, G.; Li, G.; Ma, H.; Fan, H.; Yu, L.; Ma, C.; Wu, X.; Deng, D.; Wei, M.; Tan, D.; Si, R.; Zhang, S.; Li, J.; Sun, L.; Tang, Z.; Pan, X.; Bao, X. Direct, Nonoxidative Conversion of Methane to Ethylene, Aromatics, and Hydrogen. *Science* **2014**, *344*, 616−619.
(18) Gaffney, A. M.; Mason, O. M. Ethylene production via Oxidative Dehydrogenation of Ethane using M1 catalyst. *Catal. Today* **2017**, *285*, 159−165.
(19) Robinson, J. C.; Weng, J.; Misicko, T. K.; Remedies, N.; Mainardi, D. S.; Xiao, Y. Non-Oxidative Coupling of Methane via Selective Passivized Catalysis. *Chem. Commun.* **2025**, *61*, 19183−19194.
(20) Li, Y.; Zhang, J. Non-Oxidative Coupling of Methane Catalyzed by Heterogeneous Catalysts Containing Singly Dispersed Metal Sites. *Catalysts* **2024**, *14*, 363.
(21) Huang, X.; Eggart, D.; Qin, G.; Sarma, B. B.; Gaur, A.; Yang, J.; Pan, Y.; Li, M.; Hao, J.; Yu, H.; Zimina, A.; Guo, X.; Xiao, J.; Grunwaldt, J.-D.; Pan, X.; Bao, X. Methyl Radical Chemistry in Non-Oxidative Methane Activation over Metal Single Sites. *Nat. Commun.* **2023**, *14*, 5716.
(22) Huang, X.; Jiao, X.; Lin, M.; Wang, K.; Jia, L.; Hou, B.; Li, D. Coke Distribution Determines the Lifespan of a Hollow Mo/HZSM-5 Capsule Catalyst in CH4 Dehydroaromatization. *Catal. Sci. Technol.* **2018**, *8*, 5740−5749.
(23) Julian, I.; Hueso, J. L.; Lara, N.; Solé-Daurá, A.; Poblet, J. M.; Mitchell, S. G.; Mallada, R.; Santamaría, J. Polyoxometalates as Alternative Mo Precursors for Methane Dehydroaromatization on Mo/ZSM-5 and Mo/MCM-22 Catalysts. *Catal. Sci. Technol.* **2019**, *9*, 5927−5942.
(24) Agote-Arán, M.; Fletcher, R. E.; Briceno, M.; Kroner, A. B.; Sazanovich, I. V.; Slater, B.; Rivas, M. E.; Smith, A. W. J.; Collier, P.; Lezcano-González, I.; Beale, A. M. Implications of the Molybdenum Coordination Environment in MFI Zeolites on Methane Dehydroaromatisation Performance. *Chem. Catal. Chem.* **2020**, *12*, 294−304.
(25) Julian, I.; Roedern, M. B.; Hueso, J. L.; Irusta, S.; Baden, A. K.; Mallada, R.; Davis, Z.; Santamaria, J. Supercritical solvothermal Synthesis under Reducing Conditions to Increase Stability and Durability of Mo/ZSM-5 Catalysts in Methane Dehydroaromatization. *Appl. Catal., B* **2020**, *263*, 118360.
(26) Wang, D.; Lunsford, J. H.; Rosynek, M. P. Catalytic Conversion of Methane to Benzene over Mo/ZSM-5. *Top. Catal.* **1996**, *3*, 289−297.
(27) Xie, P.; Pu, T.; Nie, A.; Hwang, S.; Purdy, S. C.; Yu, W.; Su, D.; Miller, J. T.; Wang, C. Nanoceria-Supported Single-Atom Platinum Catalysts for Direct Methane Conversion. *ACS Catal.* **2018**, *8*, 4044−4048.
(28) Xiao, Y.; Varma, A. Highly Selective Nonoxidative Coupling of Methane over Pt-Bi Bimetallic Catalysts. *ACS Catal.* **2018**, *8*, 2735−2740.
(29) Zhu Chen, J.; Wu, Z.; Zhang, X.; Choi, S.; Xiao, Y.; Varma, A.; Liu, W.; Zhang, G.; Miller, J. T. Identification of the Structure of the Bi Promoted Pt Non-Oxidative Coupling of Methane Catalyst: A Nanoscale Pt3 Bi Intermetallic Alloy. *Catal. Sci. Technol.* **2019**, *9*, 1349−1356.
(30) Zhu, P.; Bian, W.; Liu, B.; Deng, H.; Wang, L.; Huang, X.; Spence, S. L.; Lin, F.; Duan, C.; Ding, D.; Dong, P.; Ding, H. Direct Conversion of Methane to Aromatics and Hydrogen via a Heterogeneous Trimetallic Synergistic Catalyst. *Nat. Commun.* **2024**, *15*, 3280.
(31) Guczi, L.; Sarma, K. V.; Borkó, L. Non-Oxidative Methane Coupling over Co-Pt/NaY Bimetallic Catalysts. *Catal. Lett.* **1996**, *39*, 43−47.
(32) Talpade, A. D.; Canning, G.; Zhuchen, J.; Arvay, J.; Watt, J.; Miller, J. T.; Datye, A.; Ribeiro, F. H. Catalytic Reactivity of Pt Sites for Non-Oxidative Coupling of Methane (NOCM). *Chem. Eng. J.* **2024**, *481*, 148675.
(33) Malola, S.; Svelle, S.; Bleken, F. L.; Swang, O. Detailed Reaction Paths for Zeolite Dealumination and Desilication From Density Functional Calculations. *Angew. Chem., Int. Ed.* **2012**, *51*, 652−655.
(34) Mancinelli, M.; Precisvalle, N.; Ardit, M.; Beltrami, G.; Gigli, L.; Catizzone, E.; Migliori, M.; Giordano, G.; Martucci, A. Thermal Stability of Templated ZSM-5 Zeolites: An in-situ Synchrotron X-ray Powder Diffraction Study. *Microporous Mesoporous Mater.* **2023**, *362*, 112777.
(35) Wang, H.-Z.; Sun, L.-L.; Sui, Z.-J.; Zhu, Y.-A.; Ye, G.-H.; Chen, D.; Zhou, X.-G.; Yuan, W.-K. Coke Formation on Pt−Sn/Al2O3 Catalyst for Propane Dehydrogenation. *Ind. Eng. Chem. Res.* **2018**, *57*, 8647−8654.
(36) Biswas, S.; Cokas, J.; Gee, W.; Paul, D.; Dias, N.; Morgan, H. W. T.; Finn, M. T.; Hudak, B. M.; Godbold, P. M.; Klug, C. A.; Epshteyn, A.; Alexandrova, A. N.; Ahmed, M.; Kaiser, R. I. Unconventional Low Temperature Decomposition of a Saturated Hydrocarbon over Atomically-Dispersed Titanium-Aluminum-Boron Catalyst. *Nat. Commun.* **2025**, *16*, 6793.
(37) Biswas, S.; Paul, D.; Dias, N.; Kunzler, K.; Ahmed, M.; Pantoya, M. L.; Kaiser, R. I. Stress-Alteration Enhancement of the Reactivity of Aluminum Nanoparticles in the Catalytic Decomposition of exo-Tetrahydrodicyclopentadiene (JP-10). *J. Phys. Chem. A* **2024**, *128*, 3613−3624.
(38) Biswas, S.; Paul, D.; Dias, N.; Lu, W.; Ahmed, M.; Pantoya, M. L.; Kaiser, R. I. Efficient Oxidative Decomposition of Jet-Fuel exo-Tetrahydrodicyclopentadiene (JP-10) by Aluminum Nanoparticles in a Catalytic Microreactor: An Online Vacuum Ultraviolet Photoionization Study. *J. Phys. Chem. A* **2024**, *128*, 1665−1684.
(39) Biswas, S.; Paul, D.; He, C.; Dias, N.; Ahmed, M.; Pantoya, M. L.; Kaiser, R. I. Counterintuitive Catalytic Reactivity of the Aluminum Oxide "Passivation" Shell of Aluminum Nanoparticles Facilitating the Thermal Decomposition of exo-Tetrahydrodicyclopentadiene (JP-10). *J. Phys. Chem. Lett.* **2023**, *14*, 9341−9350.
(40) Paul, D.; Biswas, S.; Dias, N.; Finn, M. T.; Lipton, A. S.; Epshteyn, A.; Ahmed, M.; Kaiser, R. I. A Synchrotron-Based Vacuum Ultraviolet Photoionization Mass Spectrometer-Coupled Microreactor To Probe Thermocatalysis. *Anal. Chem.* **2025**, *97*, 22846−22857.
(41) Huang, Z.-Q.; He, S.-Y.; Ban, T.; Gao, X.; Xu, Y.-H.; Chang, C.-R. Mechanistic and Microkinetic Study of Nonoxidative Coupling of Methane on Pt-Cu Alloy Catalysts: From Single-Atom Sites to Single-Cluster Sites. *Chin. J. Catal.* **2023**, *48*, 90−100.
(42) Finn, M. T.; Chaloux, B. L.; Epshteyn, A. Exploring the Effects of Reaction Conditions on Morphology and Stability of Sonochemically Generated Ti−Al−B Fuel Powders. *Energy Fuels* **2020**, *34*, 11373−11380.
(43) Brotton, S. J.; Perera, S. D.; Misra, A.; Kleimeier, N. F.; Turner, A. M.; Kaiser, R. I.; Palenik, M.; Finn, M. T.; Epshteyn, A.; Sun, B.-J.; Zhang, L.-J.; Chang, A. H. H. Combined Spectroscopic and Computational Investigation on the Oxidation of exo-Tetrahydrodicyclopentadiene (JP-10; C10H16) Doped with Titanium−Aluminum−Boron Reactive Metal Nanopowder. *J. Phys. Chem. A* **2022**, *126*, 125−144.
(44) Góbi, S.; Lin, Z.; Zhu, C.; Head-Gordon, M.; Kaiser, R. I. Oxygen Isotope Exchange between Carbon Dioxide and Iron Oxides on Mars' Surface. *J. Phys. Chem. Lett.* **2022**, *13*, 2600−2606.
(45) Liu, L.; Corma, A. Metal Catalysts for Heterogeneous Catalysis: From Single Atoms to Nanoclusters and Nanoparticles. *Chem. Rev.* **2018**, *118*, 4981−5079.
(46) Castleman, A. W. Cluster Structure and Reactions: Gaining Insights into Catalytic Processes. *Catal. Lett.* **2011**, *141*, 1243−1253.

https://doi.org/10.1021/jacs.6c01503
J. Am. Chem. Soc. 2026, 148, 10205−10215

(47) Wang, L.; Liu, H.; Zhuang, J.; Wang, D. Small-Scale Big Science: From Nano- to Atomically Dispersed Catalytic Materials. *Small Sci.* **2022**, *2*, 2200036.
(48) El Berch, J. N.; Salem, M.; Mpourmpakis, G. Advances in Simulating Dilute Alloy Nanoparticles for Catalysis. *Nanoscale* **2025**, *17*, 1936−1953.
(49) Guo, H.; Sautet, P.; Alexandrova, A. N. Reagent-Triggered Isomerization of Fluxional Cluster Catalyst via Dynamic Coupling. *J. Phys. Chem. Lett.* **2020**, *11*, 3089−3094.
(50) Becke, A. D. Density-Functional Exchange-Energy Approximation with Correct Asymptotic Behavior. *Phys. Rev. A:At., Mol., Opt. Phys.* **1988**, *38*, 3098−3100.
(51) Lee, C.; Yang, W.; Parr, R. G. Development of the Colle-Salvetti Correlation-Energy Formula into a Functional of the Electron Density. *Phys. Rev. B* **1988**, *37*, 785−789.
(52) Weigend, F.; Ahlrichs, R. Balanced Basis Sets of Split Valence, Triple Zeta Valence and Quadruple Zeta Valence Quality for H to Rn: Design and Assessment of Accuracy. *Phys. Chem. Chem. Phys.* **2005**, *7*, 3297−3305.
(53) Weigend, F. Accurate Coulomb-Fitting Basis Sets for H to Rn. *Phys. Chem. Chem. Phys.* **2006**, *8*, 1057−1065.
(54) Grimme, S.; Antony, J.; Ehrlich, S.; Krieg, H. A Consistent and Accurate ab initio Parametrization of Density Functional Dispersion Correction (DFT-D) for the 94 Elements H-Pu. *J. Chem. Phys.* **2010**, *132*, 154104.
(55) Grimme, S.; Ehrlich, S.; Goerigk, L. Effect of the Damping Function in dispersion Corrected Density Functional Theory. *J. Comput. Chem.* **2011**, *32*, 1456−1465.
(56) Henkelman, G.; Jónsson, H. Improved Tangent Estimate in the Nudged Elastic Band Method for Finding Minimum Energy Paths and Saddle Points. *J. Chem. Phys.* **2000**, *113*, 9978−9985.
(57) Henkelman, G.; Uberuaga, B. P.; Jónsson, H. A Climbing Image Nudged Elastic Band Method for Finding Saddle Points and Minimum Energy Paths. *J. Chem. Phys.* **2000**, *113*, 9901−9904.
(58) Kozuch, S.; Shaik, S. How to Conceptualize Catalytic Cycles? The Energetic Span Model. *Acc. Chem. Res.* **2011**, *44*, 101−110.
(59) Sinn, H.; Kaminsky, W. Ziegler-Natta Catalysis. In *Adv. Organomet. Chem.*; Stone, F. G. A., West, R., Eds.; Academic Press, 1980; Vol. *18*, pp 99−149.
(60) Zhang, Z.; Cui, Z.-H.; Jimenez-Izal, E.; Sautet, P.; Alexandrova, A. N. Hydrogen Evolution on Restructured B-Rich WB: Metastable Surface States and Isolated Active Sites. *ACS Catal.* **2020**, *10*, 13867−13877.

https://doi.org/10.1021/jacs.6c01503
J. Am. Chem. Soc. 2026, 148, 10205−10215